Monthly Notices of the ROYAL ASTRONOMICAL SOCIETY

MNRAS **513,** 2349–2359 (2022) https://doi.org/10.1093/mnras/stac1081
Advance Access publication 2022 April 27

# SHARP – VIII. J0924+0219 lens mass distribution and time-delay prediction through adaptive-optics imaging

Geoff C.-F. Chen,[1★] Christopher D. Fassnacht,[2] Sherry H. Suyu,[3,4,5] Léon V. E. Koopmans,[6] David J. Lagattuta,[7,8] John P. McKean,[6,9] Matt W. Auger,[10] Simona Vegetti[3] and Tommaso Treu[1]

[1]*Department of Physics and Astronomy, University of California, Los Angeles, CA 90095, USA*
[2]*Department of Physics and Astronomy, University of California, Davis, CA 95616, USA*
[3]*Max Planck Institute for Astrophysics, Karl-Schwarzschild-Strasse 1, D-85740 Garching, Germany*
[4]*Physik Department, Technische Universität München, James-Franck-Strasse 1, D-85748 Garching, Germany*
[5]*Academia Sinica Institute of Astronomy and Astrophysics (ASIAA), 11F of ASMAB, No.1, Section 4, Roosevelt Road, Taipei 10617, Taiwan*
[6]*Kapteyn Astronomical Institute, University of Groningen, PO Box 800, NL-9700 AV Groningen, the Netherlands*
[7]*Centre for Extragalactic Astronomy, Durham University, South Road, Durham DH1 3LE, UK*
[8]*Institute for Computational Cosmology, Durham University, South Road, Durham DH1 3LE, UK*
[9]*ASTRON, Netherlands Institute for Radio Astronomy, PO Box 2, NL-7990 AA Dwingeloo, the Netherlands*
[10]*Institute of Astronomy, University of Cambridge, Madingley Road, Cambridge CB3 0HA, UK*

Accepted 2022 February 22. Received 2022 February 21; in original form 2021 August 1

## ABSTRACT

Strongly lensed quasars can provide measurements of the Hubble constant ($H_0$) independent of any other methods. One of the key ingredients is exquisite high-resolution imaging data, such as *Hubble Space Telescope* (*HST*) imaging and adaptive-optics (AO) imaging from ground-based telescopes, which provide strong constraints on the mass distribution of the lensing galaxy. In this work, we expand on the previous analysis of three time-delay lenses with AO imaging (RX J1131−1231, HE 0435−1223, and PG 1115+080), and perform a joint analysis of J0924+0219 by using AO imaging from the Keck telescope, obtained as part of the Strong lensing at High Angular Resolution Program (SHARP) AO effort, with *HST* imaging to constrain the mass distribution of the lensing galaxy. Under the assumption of a flat $\Lambda$ cold dark matter ($\Lambda$CDM) model with fixed $\Omega_{\rm m} = 0.3$, we show that by marginalizing over two different kinds of mass models (power-law and composite models) and their transformed mass profiles via a mass-sheet transformation, we obtain $\Delta t_{\rm BA} = 6.89^{+0.8}_{-0.7}\,h^{-1}\hat{\sigma}_v^2$ d, $\Delta t_{\rm CA} = 10.7^{+1.6}_{-1.2}\,h^{-1}\hat{\sigma}_v^2$ d, and $\Delta t_{\rm DA} = 7.70^{+1.0}_{-0.9}\,h^{-1}\hat{\sigma}_v^2$ d, where $h = H_0/100\,{\rm km\,s^{-1}\,Mpc^{-1}}$ is the dimensionless Hubble constant and $\hat{\sigma}_v = \sigma_v^{\rm ob}/(280\,{\rm km\,s^{-1}})$ is the scaled dimensionless velocity dispersion. Future measurements of time delays with 10 per cent uncertainty and velocity dispersion with 5 per cent uncertainty would yield a $H_0$ constraint of ∼15 per cent precision.

**Key words:** gravitational lensing: strong – instrumentation: adaptive optics – distance scale.

## 1 INTRODUCTION

Measuring the Hubble constant is one of the most important tasks in modern cosmology, especially since not only does it set the age, the size, and the critical density of the Universe, but also the recent direct $H_0$ measurements from Type Ia supernovae (SNe Ia), calibrated by the traditional Cepheid distance ladder (SH0ES Collaboration; Riess et al. 2019), show a 4.4$\sigma$ tension with the *Planck* results under the assumption of the $\Lambda$ cold dark matter ($\Lambda$CDM) model (e.g. Komatsu et al. 2011; Hinshaw et al. 2013; Anderson et al. 2014; Kazin et al. 2014; Ross et al. 2015; Planck Collaboration VI 2020). However, a recent measurement of $H_0$ from SNe Ia calibrated by the tip of the red-giant branch (TRGB) by the Carnegie–Chicago Hubble Program (CCHP) agrees with both the *Planck* and SH0ES results within the errors (Freedman et al. 2019, 2020). These results clearly demonstrate that it is crucial to test any single measurement by independent probes.

Strongly lensed quasars provide an independent way to measure the Hubble constant (Refsdal 1964; Treu & Marshall 2016; Suyu et al. 2017). With the combination of time delays, high-resolution imaging, the velocity dispersion of the lensing galaxy, and the description of the mass along the line of sight [so-called external mass-sheet transformation (MST); see details in Falco, Gorenstein & Shapiro 1985; Gorenstein, Falco & Shapiro 1988; Fassnacht et al. 2002; Collett et al. 2013; Greene et al. 2013; Suyu et al. 2013], the Time-Delay Cosmography (TDCOSMO)[1] Collaboration (Millon et al. 2020) has shown that one can provide robust constraints on both the angular diameter distance to the lens ($D_{\rm d}$; Jee, Komatsu & Suyu 2015) and the time-delay distance that is a ratio of the angular diameter distances in the system:

$$D_{\Delta t} \equiv (1+z_{\rm d})\frac{D_{\rm d}D_{\rm s}}{D_{\rm ds}} \propto H_0^{-1}, \tag{1}$$

where $z_{\rm d}$ is the redshift of the lens, $D_{\rm s}$ is the distance to the background source, and $D_{\rm ds}$ is the distance between the lens and

★ E-mail: gcfchen@astro.ucla.edu

[1]http://www.tdcosmo.org/

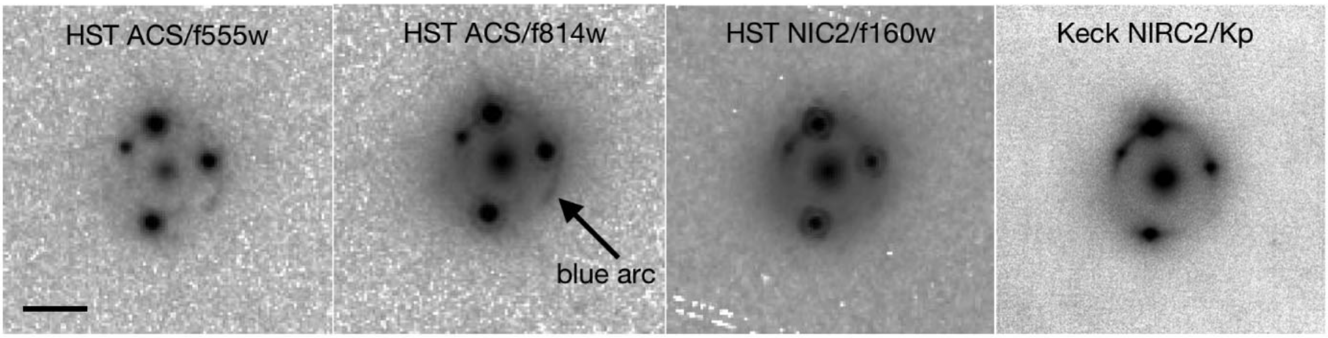


**Figure 1.** *HST* and AO images of J0924+0219 gravitational lens systems. The solid horizontal line represents 1 arcsec scale. The foreground main lens is located in the centre of the lens system. The multiple lensed images and the extended arc around the lensing galaxy are from the background active galactic nucleus (AGN) and its host galaxy.

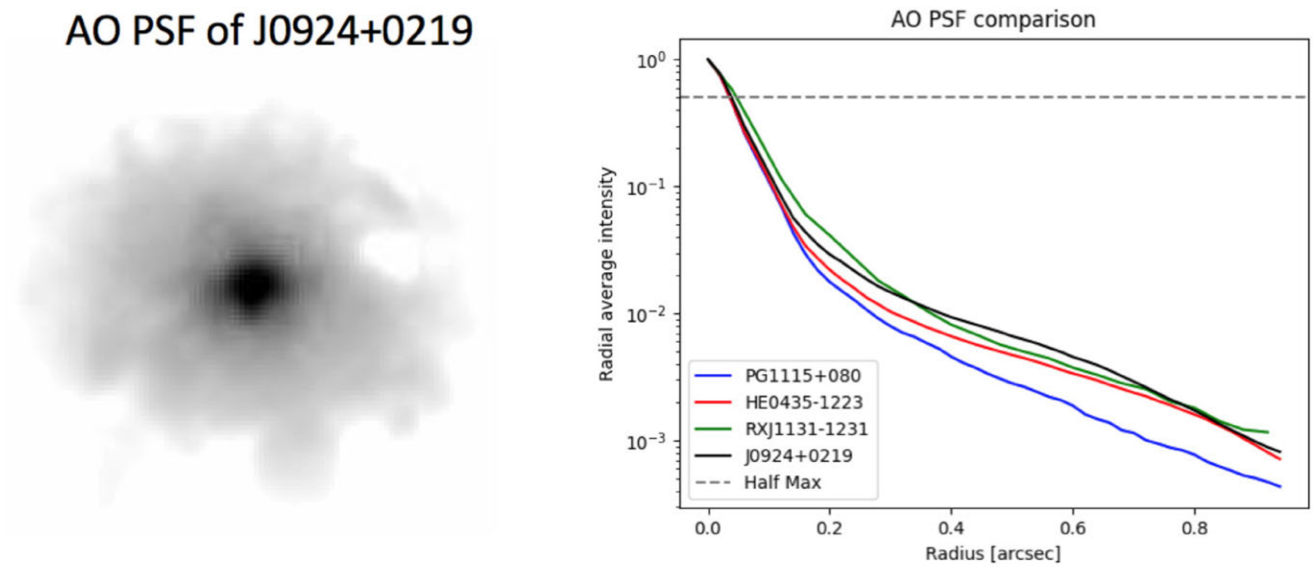


**Figure 2.** The left-hand panel is the reconstructed AO PSF of J0924+0219. The right-hand panel is the comparison of the radial average intensity of the reconstructed PSFs from all four AO lenses from previous work (Chen et al. 2019). All the reconstructed PSFs show core structures and extended wings.

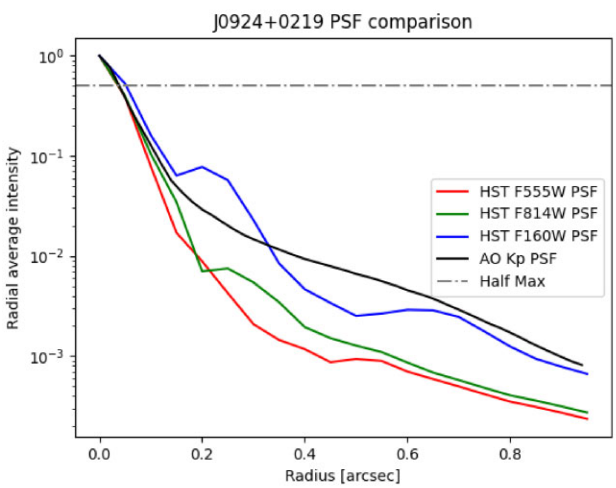


**Figure 3.** The comparison of the radial average intensity of the reconstructed AO PSFs and *HST* PSF of J0924+0219.

the source. These distances are used to determine cosmological parameters (e.g. Suyu et al. 2014; Bonvin et al. 2016; Birrer et al. 2019; Chen et al. 2019; Jee et al. 2019; Rusu et al. 2019; Taubenberger et al. 2019; Shajib et al. 2020; Wong et al. 2020), primarily $H_0$.

A blind analysis done by Wong et al. (2020) with this technique as part of the H0 Lenses in COSMOGRAIL's Wellspring (H0LiCOW) program (Suyu et al. 2017), in collaboration with the COSmological MOnitoring of GRAvItational Lenses (COSMOGRAIL; e.g. Courbin et al. 2018) and Strong lensing at High Angular Resolution Program (SHARP; Chen et al. 2019; Fassnacht et al., in preparation) programs, combined the data from six gravitational lens systems,[2] and inferred $H_0 = 73.3^{+1.7}_{-1.8}\,\mathrm{km\,s^{-1}\,Mpc^{-1}}$, a value that was 3.8$\sigma$ away from the *Planck* results. The above work marginalized over two different kinds of mass profiles for the lensing galaxies in order to better estimate the uncertainties. The first description consists of a Navarro–Frenk–White (NFW) dark matter halo (Navarro, Frenk & White 1996) plus a constant mass-to-light (M/L) ratio stellar distribution (the 'composite

[2]Except the first lens, B1608+656, which was not done blindly, the lenses in H0LiCOW are analysed blindly with respect to the cosmological quantities of interest.

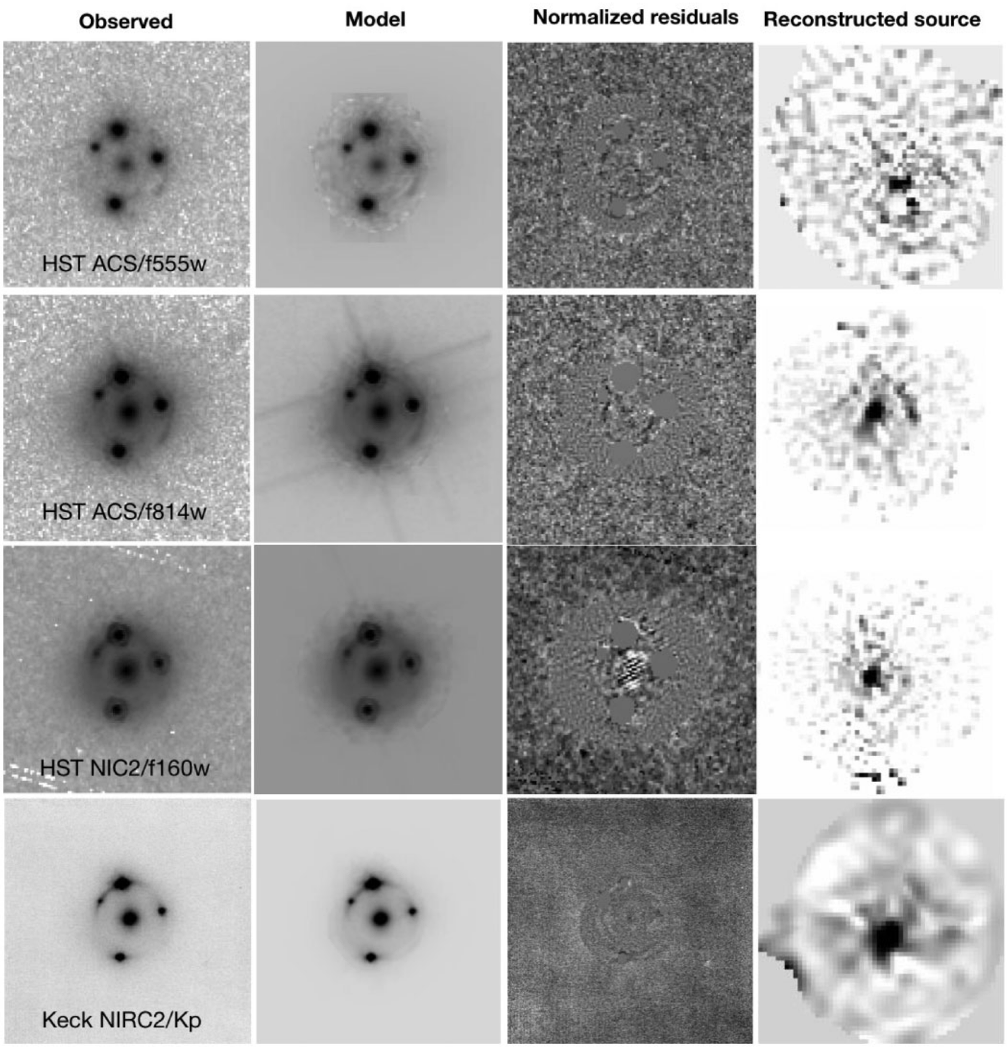


**Figure 4.** J0924+0219 *HST* and AO image reconstruction of the most probable model with a source grid of 53 × 53 pixels. We use 59 × 59 pixels of the AO PSF and 29 × 29 pixels of the *HST* PSF for convolution of spatially extended images. From left column to right column: observed imaging, model imaging, normalized residuals, and reconstructed source.

**Table 1.** Lens model parameters for power-law model.

| Description | Parameter | Marginalized constraints |
|---|---|---|
| Lens mass distribution | | |
| Centroid of G in $\theta_1$ (arcsec) | $\theta_1$ | $3.01^{+0.08}_{-0.05}$ |
| Centroid of G in $\theta_2$ (arcsec) | $\theta_2$ | $3.02^{+0.03}_{-0.04}$ |
| Axis ratio of G | $q$ | $0.61 \pm 0.01$ |
| Position angle of G | $\theta$ | $-0.04 \pm 0.01$ |
| Einstein radius of G (arcsec) | $\theta_{\rm E}$ | $0.940^{+0.004}_{-0.003}$ |
| Radial slope of G | $\gamma$ | $2.270^{+0.007}_{-0.003}$ |
| External shear strength | $\gamma^{'}$ | $0.017^{+0.001}_{-0.003}$ |
| External shear angle | $\theta_{\gamma'}$ | $4.24^{+0.01}_{-0.03}$ |

*Note.* The source pixel parameters are marginalized. The confidence interval represents 1$\sigma$ uncertainty. Position angle is counterclockwise from +x in radians.

model'). The second description models the three-dimensional total mass density distribution, i.e. luminous plus dark matter, of the galaxy as a power law (Barkana 1998), i.e. $\rho(r) \propto r^{-\gamma}$ (the power-law model). Millon et al. (2020) later combined six lenses from Wong et al. (2020) with one additional lens analysed by Shajib et al. (2020) in the STRong lensing Insights into the Dark Energy Survey (STRIDES) program (Treu et al. 2018), and showed that even if we separate these two descriptions of the mass distribution of the lensing galaxy, the $H_0$ measurements are consistent well within 1 per cent. An independent check by Chen et al. (2019) using ground-based high-resolution adaptive-optics (AO) imaging data from SHARP[3] with three strongly lensed quasar also shows consistent results with Wong et al. (2020) and is 3.5$\sigma$ away from *Planck* results.

Given the growing statistical tension between $H_0$ measurements, efforts by the TDCOSMO Collaboration have gone into studying potential systematic uncertainties (Gilman, Birrer & Treu 2020; Millon et al. 2020). A crucial potential source of uncertainty is the assumptions on the radial density profile. Birrer et al. (2020) introduced a flexible parametrization on the mass model that is maximally degenerate with $H_0$ through the MST (so-called internal MST; see also Schneider & Sluse 2013; Xu et al. 2016; Kochanek 2020, 2021; Chen et al. 2021b), as a way to express departures from

[3]The Keck AO imaging data are part of the SHARP (Fassnacht et al., in preparation).

**Table 2.** Lens light model parameters for power-law model.

| Description<br>Lens light as Sérsic profiles | Parameter | F555W | F814W | F160W | Keck AO |
|---|---|---|---|---|---|
| Centroid of S in $\theta_1$ (arcsec) | $\theta_{1,\mathrm{Light}}$ | $3.0092 \pm 0.0002$ | $3.0092 \pm 0.0002$ | $3.0092 \pm 0.0002$ | $3.0092 \pm 0.0002$ |
| Centroid of S in $\theta_2$ (arcsec) | $\theta_{2,\mathrm{Light}}$ | $2.9935 \pm 0.0002$ | $2.9935 \pm 0.0002$ | $2.9935 \pm 0.0002$ | $2.9935 \pm 0.0002$ |
| Axis ratio of S1 | $q_{\mathrm{S1}}$ | $0.88^{+0.03}_{-0.04}$ | $0.67^{+0.02}_{-0.03}$ | $0.89^{+0.02}_{-0.01}$ | $0.76 \pm 0.03$ |
| Position angle of S1 | $\theta_{\mathrm{S1}}$ | $208 \pm 23$ | $285 \pm 3$ | $128 \pm 6$ | $107 \pm 5$ |
| Amplitude of S1 | $I_{\mathrm{s,\,S1}}$ | $0.2 \pm 0.2$ | $0.071^{+0.004}_{-0.01}$ | $0.669^{+0.005}_{-0.007}$ | $0.41 \pm 0.02$ |
| Effective radius of S1 (arcsec) | $R_{\mathrm{eff,\,S1}}$ | $0.105 \pm 0.005$ | $0.95 \pm 0.03$ | $0.112 \pm 0.001$ | $0.96 \pm 0.03$ |
| Index of S1 | $n_{\mathrm{S1}}$ | $0.6 \pm 0.1$ | $0.9 \pm 0.1$ | $1.25 \pm 0.02$ | $0.366^{+0.005}_{-0.007}$ |
| Axis ratio of S2 | $q_{\mathrm{S2}}$ | $0.93 \pm 0.05$ | $0.89^{+0.04}_{-0.08}$ | $0.76 \pm 0.05$ | $0.82^{+0.05}_{-0.06}$ |
| Position angle of S2 | $\theta_{\mathrm{S2}}$ | $-44 \pm 6$ | $294 \pm 12$ | $-58 \pm 4$ | $172 \pm 6$ |
| Amplitude of S2 | $I_{\mathrm{s,\,S2}}$ | $0.00632^{+0.00008}_{-0.0004}$ | $2.1 \pm 0.1$ | $0.023^{+0.002}_{-0.001}$ | $6.3^{+1.5}_{-2.2}$ |
| Effective radius of S2 (arcsec) | $R_{\mathrm{eff,\,S2}}$ | $1.3 \pm 0.1$ | $0.104^{+0.007}_{-0.004}$ | $0.79^{+0.04}_{-0.07}$ | $0.145 \pm 0.01$ |
| Index of S2 | $n_{\mathrm{S2}}$ | $3.2^{+0.4}_{-0.6}$ | $1.1^{+0.1}_{-0.1}$ | $0.368 \pm 0.003$ | $0.9 \pm 0.2$ |
| Axis ratio of S3 | $q_{\mathrm{S3}}$ | – | $0.52^{+0.08}_{-0.04}$ | – | $0.7 \pm 0.1$ |
| Position angle of S3 | $\theta_{\mathrm{S3}}$ | – | $358 \pm 3$ | – | $-256 \pm 12$ |
| Amplitude of S3 | $I_{\mathrm{s,\,S3}}$ | – | $0.29 \pm 0.05$ | – | $0.29 \pm 0.05$ |
| Effective radius of S3 (arcsec) | $R_{\mathrm{eff,\,S3}}$ | – | $0.27 \pm 0.01$ | – | $0.28 \pm 0.01$ |
| Index of S3 | $n_{\mathrm{S3}}$ | – | $0.6^{+0.2}_{-0.1}$ | – | $0.5^{+0.2}_{-0.1}$ |

*Note.* The lens lights of all four bands share the common centroid. The source pixel parameters are marginalized and are thus not listed. The confidence interval represents $1\sigma$ uncertainty. Position angle is in degree (N→E).

the standard assumptions in previous work (Blum, Castorina & Simonović 2020; Shajib et al. 2021) and validated it with the time-delay modelling challenge (Ding et al. 2021). With this parametrization, the main factor determining the precision of the cosmological inference is the stellar kinematics in the lensing galaxy (see discussion by Treu & Koopmans 2002; Koopmans et al. 2003; Birrer, Amara & Refregier 2016; Jee et al. 2016; Chen et al. 2021b). With the MST parametrization, the uncertainty on $H_0$ based on the seven lens sample of Millon et al. (2020) goes from $\sim$2 per cent to $\sim$8 per cent, in a standard $\Lambda$CDM cosmology.

To further constrain the $H_0$ value contributed from the MST and anisotropy parameters, Birrer et al. (2020) developed a hierarchical Bayesian framework by including external data sets, assuming they are drawn from the same parent population. When assuming that the TDCOSMO lenses and the Sloan Lens ACS Survey (SLACS; Bolton et al. 2004, 2006; Auger et al. 2010) samples are drawn from a single stellar-orbit anisotropy distribution, Birrer et al. (2020) inferred $73.3 \pm 5.8\,\mathrm{km\,s^{-1}\,Mpc^{-1}}$. Assuming that TDCOSMO and SLACS are also drawn from the same population in terms of both anisotropy and mass density profile, the inference on $H_0$ shifted to $67.4^{+4.1}_{-3.2}\,\mathrm{km\,s^{-1}\,Mpc^{-1}}$, which statistically agrees with both *Planck* and SH0ES results. Increasing the number of the time-delay lens systems and using different external data sets are crucial to assess whether the difference between SLACS and TDCOSMO is real or a statistical fluctuation (Birrer & Treu 2021).

To expand the sample of analysed AO-observed time-delay lenses (Chen et al. 2019), we study the J0924+0219 lens system, which has AO imaging from SHARP and archival *HST* imaging. In this work, we take into account both the internal and external MST and forecast the time delays. Since the velocity dispersion of the lensing galaxy is not yet measured, we predict the time delays based on the imaging data and an expected precision of the kinematic data. In Section 2, we describe the basic information on J0924+0219 and describe the data acquisition and analysis. In Section 3, we describe the models we used for fitting the imaging. In Section 4, we make a time-delay prediction based on imaging data under the assumption of a flat $\Lambda$CDM model with fixed $\Omega_{\mathrm{m}} = 0.3$. The conclusion is in Section 5.

## 2 J0924+0219

The J0924+0219 system (J2000: $09^{\mathrm{h}}24^{\mathrm{m}}55\overset{\mathrm{s}}{.}87$, $02^{\circ}19'24\overset{''}{.}9$) is a quadruply lensed quasar discovered by Inada et al. (2003). The main lensing galaxy is at a redshift of $z_{\mathrm{d}} = 0.394 \pm 0.001$ (Eigenbrod et al. 2006), and the source redshift is $z_{\mathrm{s}} = 1.524 \pm 0.001$ (Inada et al. 2003). The analysis in this paper is based on new Keck AO and archival *HST* observations of J0924+0219. We describe the data acquisition and analysis in Sections 2.1 and 2.2. We show the data from three *HST* bands and one Keck AO $K'$-band in Fig. 1.

### 2.1 *Hubble Space Telescope* imaging

We use optical and near-infrared imaging of the system obtained from the *Hubble Space Telescope* (*HST*) archive. The archival data include the Near-Infrared Camera and Multi-Object Spectrometer (NICMOS) images through the F160W filter (total exposure time: 5311.52 s) taken with *HST* on 2003 November 23 and Advanced Camera for Surveys (ACS)/Wide Field Camera (WFC) images though the F814W filter (total exposure time: 2296 s) and F555W filter (total exposure time: 2188 s) taken with *HST* on 2003 November 18 (PID: 9744, PI: Kochanek). We process the data using AstroDrizzlewith standard settings, which removes the geometric distortions, corrects for sky background variations, and flags cosmic rays. The final drizzled *HST* images with a scale of 0.05 arcsec pixel$^{-1}$ are presented in Fig. 1.

### 2.2 Keck adaptive-optics imaging

The adaptive-optics (AO) imaging was obtained at $K'$-band with the Near-Infrared Camera 2 (NIRC2), as part of the SHARP AO effort (Fassnacht et al., in preparation). The target was observed with the

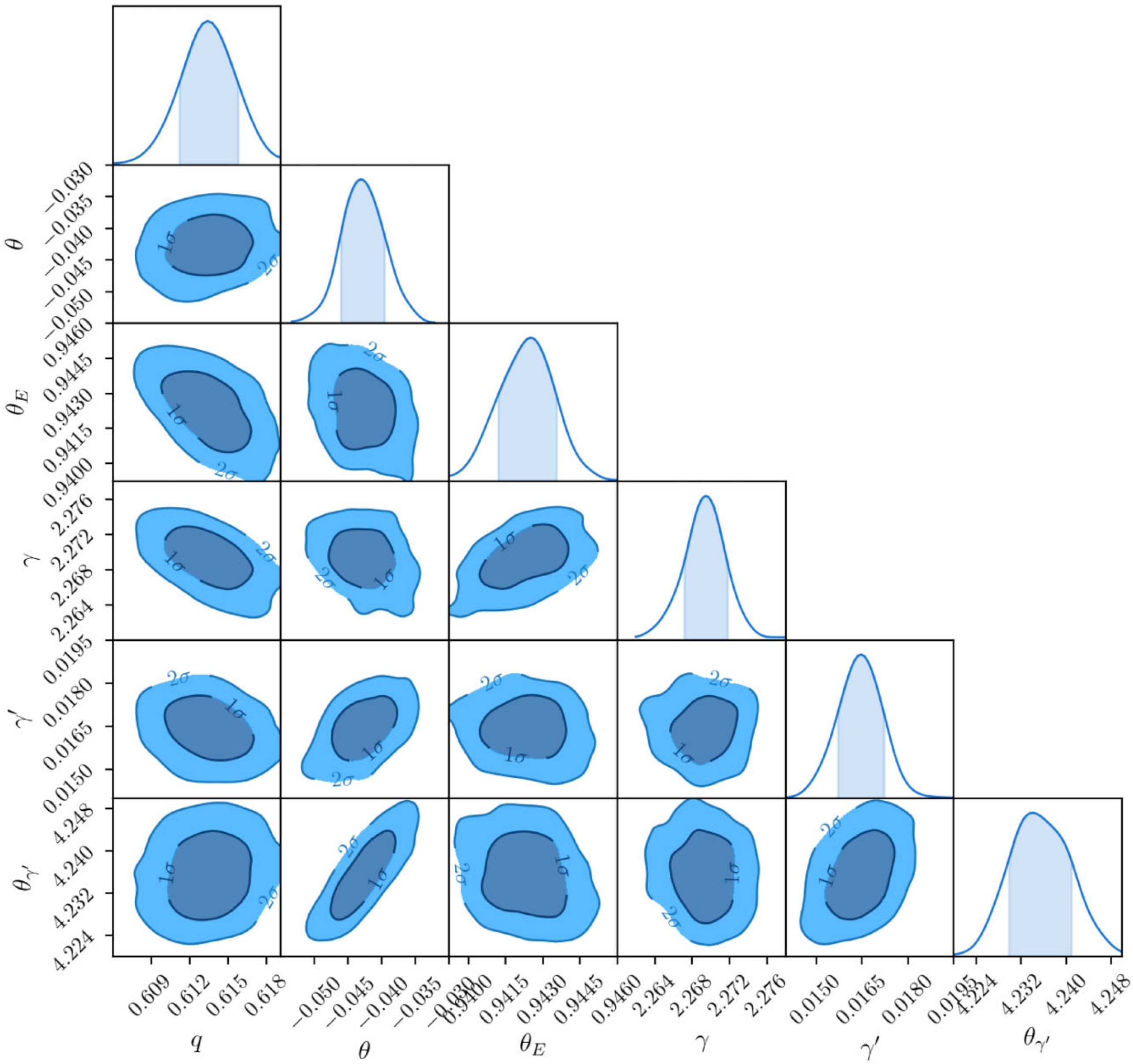


**Figure 5.** Marginalized mass-model parameter distributions from the J0924+0219 power-law lens model results. The description of the parameters is as follows: $q$ is axial ratio of power-law mass profile, $\theta$ is the position angle of power-law mass profile, $\theta_{\mathrm{E}}$ is the Einstein radius, $\gamma$ is the slope, $\gamma^{'}$ is the strength of the external shear, and $\theta_{\gamma'}$ is the orientation of the shear strength. The contours represent the 68.3 per cent and 95.4 per cent quantiles. Position angle is counterclockwise from +x in radians.

narrow camera set-up, which provides a roughly $10 \times 10$ arcsec$^2$ field of view and a pixel scale of 9.942 milliarcsec (mas). There are three exposures of 300 s on 2011 December 30, seven exposures of 300 s on 2012 May 16, and four exposures of 300 s on 2012 May 18. The total exposure time was 4200 s. We follow our previous work (Chen et al. 2016, 2019) and use the SHARP PYTHON-based pipeline, which performs a flat-field correction, sky subtraction, correction of the optical distortion in the images, and a coaddition of the exposures. For the distortion correction step, the images are resampled to produce final pixel scales of 10 mas pixel$^{-1}$ for the narrow camera. The narrow camera pixels samples well the AO .point spread function (PSF), which has typical full width at half-maximum (FWHM) values of 60–90 mas. To improve the modelling efficiency for the narrow camera data, we perform a $2 \times 2$ binning of the images produced by the pipeline to obtain images that have a 20 mas pixel$^{-1}$ scale. The final Keck AO images are presented in Fig. 1.

## 3 J0924+0219 MODELLING

We describe the PSF models in Section 3.1, lens modelling in Section 3.2, kinematics modelling in Section 3.3, and time-delay prediction model in Section 3.4.

### 3.1 The PSF of J0924

For the F160W band *HST* imaging, we use TINYTIM (Krist & Hook 1997) to generate the PSFs with different spectral index, $\hat{\eta}_v$, of a

**Table 3.** Lens mass model parameters for composite model. The baryonic component are described by two chameleon profiles that mimic the Sérsic profiles. Each chameleon profile is composed of two cored isothermal profiles. We label the two chameleon profiles as B1 and B2.

| Description | Parameter | Marginalized or optimized constraints |
|---|---|---|
| Lens mass distribution | | |
| Mass-to-light ratio | M/L | $5.4 \pm 0.2$ |
| Centroid of B1 in $\theta_1$ (arcsec) | $\theta_{1,\mathrm{B1}}$ | $3.0096 \pm 0.0002$ |
| Centroid of B1 in $\theta_2$ (arcsec) | $\theta_{2,\mathrm{B1}}$ | $2.9906 \pm 0.0002$ |
| Axis ratio of B1 | $q_{\mathrm{B1}}$ | $0.811^{+0.007}_{-0.008}$ |
| Position angle of B1 | $\phi_{\mathrm{B1}}$ | $-33.05 \pm 0.02$ |
| Amplitude of B1 | $I_{\mathrm{s,\,B1}}$ | $2.72 \pm 0.01$ |
| Core radius 1 of B1 | $r_{\mathrm{c,\,1,\,B1}}$ | $0.105 \pm 0.002$ |
| Core radius 2 of B1 | $r_{\mathrm{c,\,2,\,B2}}$ | $0.182 \pm 0.001$ |
| Axis ratio of B2 | $q_{\mathrm{B2}}$ | $0.46 \pm 0.01$ |
| Position angle of B2 | $\phi_{\mathrm{B2}}$ | $-34.33 \pm 0.02$ |
| Amplitude of B2 | $I_{\mathrm{s,\,B2}}$ | $4.89 \pm 0.01$ |
| Core radius 1 of B2 | $r_{\mathrm{c,\,1,\,B2}}$ | $0.020 \pm 0.001$ |
| Core radius 2 of B2 | $r_{\mathrm{c,\,2,\,B2}}$ | $0.06 \pm 0.02$ |
| Centroid of NFW in $\theta_1$ (arcsec) | NFW $\theta_1$ | $2.90 \pm 0.03$ |
| Centroid of NFW in $\theta_2$ (arcsec) | NFW $\theta_2$ | $3.093^{+0.005}_{-0.05}$ |
| Axis ratio of NFW | NFW $q$ | $0.83 \pm 0.02$ |
| Position angle of NFW | NFW $\theta_q$ | $-0.11^{+0.05}_{-0.04}$ |
| Amplitude of NFW | NFW $\kappa_{\mathrm{s}}$ | $0.359 \pm 0.003$ |
| Core radius of NFW | NFW $r_{\mathrm{s}}$ (arcsec) | $11.3 \pm 0.1$ |
| External shear strength | $\gamma'$ | $0.001 \pm 0.001$ |
| External shear angle | $\theta_{\gamma'}$ | $4.3 \pm 0.1$ |

*Note.* The source pixel parameters are marginalized and are thus not listed. The confidence interval represents $1\sigma$ uncertainty. Position angle is counterclockwise from +x in radians.

power law from −0.4 to −2.5 and different focus values[4] from 0 to 10. Given the F160W band *HST* imaging, we find that the best fit to the imaging is the PSF with focus equal to 0 and spectral index equal to −1.3. We use this TINYTIM PSF as the initial guess and then apply the PSF-correction method of Chen et al. (2016) while modelling the F160W *HST* imaging. For the F814W and F555W bands, which were observed with the ACS with a larger field of view, we use one of the nearby bright stars as the initial guess of the PSF and apply the PSF correction until the residuals stabilized. For the AO imaging, we follow the criteria described in section 4.4.3 of Chen et al. (2016) and perform nine iterative steps to create the final PSF and make sure the size of the PSF for convolution is large enough ($1.18 \times 1.18$ arcsec$^2$) such that the results are stable. The FWHM of the AO PSF is ∼75 mas. The FWHM of the *HST* PSF is ∼80 mas. We show the reconstructed AO PSF in Fig. 2 and the comparison of AO and *HST* PSF in Fig. 3.

### 3.2 Lens imaging modelling

Eigenbrod et al. (2006) first modelled this system with *HST* imaging and suspected that the second set of bluer arcs in F814W band (see Fig. 1) inside and outside the area delimited by the red arcs in F160W band could be either a second source at a different redshift or a star-forming region in the source galaxy. We examine the possibility of a second source plane existing at a lower redshift than the source ($z = 1.52$) due to the bluer colour of the arc and find that the scenario is very unlikely, as the macro model determined by the red arc cannot reproduce a reasonable source for the blue arcs given a possible range of the source redshift from $z = 0.5$ to $z < 1.52$. In contrast, we do find that a star-forming region can be reconstructed at the same source redshift. Faure et al. (2011) modelled the lens with high-resolution $H$ and $K_{\mathrm{s}}$ imaging obtained using the European Southern Observatory (ESO) Very Large Telescope (VLT) with AO and the laser guide star system. They identified a luminous object, located ∼0.3 arcsec to the north of the lens galaxy, but showed that it cannot be responsible for the anomalous flux ratios. Many studies (e.g. Metcalf & Madau 2001; Bradač et al. 2002; Dalal & Kochanek 2002; Pooley et al. 2012; Schechter et al. 2014; Glikman et al. 2018; Badole et al. 2020) have shown that the macro model cannot explain the flux ratios in this lens, which suggested the presence of microlensing or dark matter substructures. Thus, to avoid possible biases caused by flux ratios, we only use the lensed quasar positions and the extended arc to constrain the mass model, which is also the standard procedure for $H_0$ measurements in TDCOSMO Collaboration. Ignoring the fluxes of the lensed quasar images will not affect the constraining power of the imaging data, since the lensed arc emission is much more constraining than the lensed quasar fluxes. In addition, For the error budget of $H_0$ contributed from the uncertainties of the lensed quasar positions, Chen et al. (2021a) have showed that with high-resolution AO imaging it is a subdominate term given configuration of the J0924+0219 lens system. Gilman et al. (2020) also show that the presence of substructures do not bias $H_0$ above the per cent level. We use GLEE, a strong lens modelling code to model (Suyu & Halkola 2010; Suyu et al. 2012) the three *HST* bands and one Keck AO band simultaneously. We describe the models in the following for fitting the high-resolution imaging data. We show the imaging, models, normalized residuals, and reconstructed sources in Fig. 4. Note that since the source in F555W band has more clumpy star-forming regions, the reconstructed source is less regular, with small-scale structures and more noise.[5] In addition, the noise-overfitting problem is due to the fact that the outer region of the source plane is under-regularized, but this effect will not affect the uncertainty because the uncertainty will be dominated by the time delay and velocity dispersion measurements. Besides, we model the imaging with different source resolutions and marginalize over them to control the systematics.

(i) *Power-law mass model + shear + Sérsic light model*. We first choose the softened power-law elliptical mass (SPEMD; Barkana 1998) density profile with a softening length close to zero – the main parameters include the radial slope ($\gamma$), Einstein radius ($\theta_{\mathrm{E}}$), position angle ($\theta_q$), and the axial ratio of the elliptical isodensity contours ($q$) – to simultaneously model the extended arcs seen in the three *HST* bands and one AO band, and reconstruct the source structure on a pixelated grid (Suyu et al. 2006). The power-law model is motivated by many studies that have shown that a power-law model provides a good description of the lensing galaxies (e.g. Koopmans et al. 2006, 2009; Suyu et al. 2009; Auger et al. 2010; Barnabè et al. 2011; Sonnenfeld et al. 2013; Cappellari et al. 2015; Shajib et al. 2021). In the modelling, we found that two concentric Sérsic profiles are

[4]The flux per unit frequency interval is $F_\nu = C\nu^{\hat{\eta}_\nu}$, where $\hat{\eta}_\nu$ is the power-law index and $C$ is a constant; focus is related to the breathing of the secondary mirror, which is between 0 and 10.

[5]See also the same effect in Wong et al. (2017).

**Table 4.** Lens model parameters for composite model.

| Description | Parameter | F555W | F814W | F160W | Keck AO |
|---|---|---|---|---|---|
| Lens light as Sérsic profiles | | | | | |
| Axis ratio of S1 | $q_{\mathrm{S1}}$ | $0.92 \pm 0.03$ | $0.67^{+0.02}_{-0.03}$ | – | $0.75 \pm 0.03$ |
| Position angle of S1 | $\phi_{\mathrm{S1}}$ | $4.9 \pm 0.2$ | $6.55^{+0.02}_{-0.06}$ | – | $-9.11^{+0.07}_{-0.08}$ |
| Amplitude of S1 | $I_{\mathrm{s,\,S1}}$ | $0.158 \pm 0.007$ | $0.072^{+0.004}_{-0.01}$ | – | $0.40 \pm 0.02$ |
| Effective radius of S1 (arcsec) | $R_{\mathrm{eff,\,S1}}$ | $0.175 \pm 0.005$ | $0.96^{+0.03}_{-0.02}$ | – | $0.96^{+0.03}_{-0.02}$ |
| Index of S1 | $n_{\mathrm{Sérsic,S1}}$ | $1.69 \pm 0.09$ | $0.86^{+0.1}_{-0.07}$ | – | $0.365^{+0.006}_{-0.007}$ |
| Axis ratio of S2 | $q_{\mathrm{S2}}$ | $0.72 \pm 0.04$ | $0.89^{+0.05}_{-0.08}$ | – | $0.83^{+0.05}_{-0.06}$ |
| Position angle of S2 | $\phi_{\mathrm{S2}}$ | $0.28 \pm 0.07$ | $6.6 \pm 0.2$ | – | $-1.7 \pm 0.1$ |
| Amplitude of S2 | $I_{\mathrm{s,\,S2}}$ | $0.0046 \pm 0.0004$ | $2.1 \pm 0.1$ | – | $6.3^{+1.5}_{-2.2}$ |
| Effective radius of S2 (arcsec) | $R_{\mathrm{eff,\,S2}}$ | $2.11^{+0.08}_{-0.07}$ | $0.100^{+0.007}_{-0.004}$ | – | $0.15 \pm 0.01$ |
| Index of S2 | $n_{\mathrm{Sérsic,S2}}$ | $1.1 \pm 0.1$ | $1.06^{+0.07}_{-0.1}$ | – | $0.9^{+0.3}_{-0.2}$ |
| Axis ratio of S3 | $q_{\mathrm{S3}}$ | – | $0.52^{+0.08}_{-0.04}$ | – | $0.7 \pm 0.1$ |
| Position angle of S3 | $\phi_{\mathrm{S3}}$ | – | $7.82^{+0.03}_{-0.04}$ | – | $-2.8 \pm 0.2$ |
| Amplitude of S3 | $I_{\mathrm{s,\,S3}}$ | – | $0.29 \pm 0.04$ | – | $0.28 \pm 0.04$ |
| Effective radius of S3 (arcsec) | $R_{\mathrm{eff,\,S3}}$ | – | $0.27 \pm 0.01$ | – | $0.27 \pm 0.02$ |
| Index of S3 | $n_{\mathrm{Sérsic,S3}}$ | – | $0.6 \pm 0.2$ | – | $0.6^{+0.3}_{-0.2}$ |

*Note.* The lens lights of all four bands share the common centroid. The source pixel parameters are marginalized and are thus not listed. S1, S2, and S3 represent three different Sérsic profiles. The confidence interval represents $1\sigma$ uncertainty. Position angle is counterclockwise from +x in radians. The lens light parameters for the F160W band are based on chameleon profiles and are used to describe the baryonic lens mass distribution through a constant M/L ratio. We use the F160W band because it probes the rest-frame near-infrared and thus should be the best tracer of stellar mass. These chameleon parameter values for F160W are listed in Table 3.

sufficient to describe the light distribution of the lensing galaxy in the *HST* F555W and *HST* F160W bands, while three concentric Sérsic profiles are needed for the *HST* F814W band and Keck AO band. Except for the parameters that describe the lens light centre ($\theta_{1,\mathrm{Light}}$ and $\theta_{2,\mathrm{Light}}$), which are linked together for the light profiles, the light parameters (position angles, ellipticities, and Sérsic indices) are free. We list all parameters in Tables 1 and 2, and show the important marginalized mass model parameters in Fig. 5.

(ii) *Composite mass model + shear + chameleon light profile*. We test a composite (baryonic + dark matter) model (e.g. Suyu et al. 2014). For the dark matter component we adopt the standard NFW profile (Navarro et al. 1996) with the following parameters: halo normalization (NFW $\kappa_{\mathrm{s}}$), halo scale radius (NFW $r_{\mathrm{s}}$), halo minor-to-major axial ratio (NFW $q$), and associated position angle (NFW $\theta_q$). This is motivated by Dutton & Treu (2014), who find that non-contracted NFW profiles are a good representation for the dark matter haloes of massive elliptical galaxies (see also Shajib et al. 2021). The baryonic component is modelled by multiplying the lens surface brightness distribution by a constant M/L ratio parameter. For computational efficiency, we model the surface brightness with chameleon profile. The chameleon profile is the difference of two isothermal profiles and is a good approximation to a Sérsic profile over the range of interest (see details in Dutton et al. 2011). We link the baryonic matter to the chameleon light profiles of the F160W bands because it probes the rest-frame near-infrared and thus should be the best tracer of stellar mass (see also Wong et al. 2017; Chen et al. 2019). Since the degeneracy between the wings of the AO PSF and lens light could bias the inferred baryonic component, we do not use AO lens light to infer the baryonic distribution (Chen et al. 2019). However, when combining with *HST* imaging, the well-known *HST* PSF can provide the information of baryonic distribution (Chen et al. 2019). Future AO imaging with AO PSF reconstructed from telemetry data can break the degeneracy and directly infer the baryonic matter distribution without the need for *HST* imaging (Chen et al. 2021a). We set a Gaussian prior of $r_{\mathrm{s}} = 15.0 \pm 2.0$ arcsec based on the results of Gavazzi et al. (2007) for lenses in the SLACS sample, which encompasses the redshift of J0924+0219. We list all parameters in Tables 3 and 4, and show the important marginalized parameters in Fig. 6. For the composite model, we list the parameters that can be used for future microlensing study (e.g. Chen et al. 2018) in Table 5.

### 3.3 Kinematic modelling

To predict the time delays under the presence of the MST, velocity dispersion information is required to constrain the normalization of the 3D deprojected mass model. For computational simplicity, we use spherical cases of these profiles. This assumption is sufficient for the quality of the measured velocity dispersions (Sonnenfeld et al. 2012). We calculate the 3D radial velocity dispersion by numerically integrating the solutions of the spherical Jeans equation (Binney & Tremaine 1987):

$$\frac{1}{\rho_*}\frac{\mathrm{d}\left(\rho_*\sigma_{\mathrm{r}}^2\right)}{\mathrm{d}r} + 2\frac{\beta_{\mathrm{ani}}\sigma_{\mathrm{r}}^2}{r} = -\frac{GM(r)}{r^2}, \quad (2)$$

where $M(r)$ follows either the power-law mass or composite model. For the stellar component, we assume a Hernquist profile (Hernquist 1990),

$$\rho_* = \frac{I_0 a}{2\pi r(r+a)^3}, \quad (3)$$

where $I_0$ is the normalization term and the scale radius can be related to the effective radius by $a = 0.551 r_{\mathrm{eff}}$. To compare with the future data, the seeing-convolved luminosity-weighted line-of-sight velocity dispersion can be expressed as

$$\left(\sigma_v^{\mathrm{P}}\right)^2 = \frac{\int_{\mathcal{A}}\left[I(R)\sigma_{\mathrm{s}}^2 * \mathcal{P}\right]\mathrm{d}\mathcal{A}}{\int_{\mathcal{A}}[I(R) * \mathcal{P}]\,\mathrm{d}\mathcal{A}}, \quad (4)$$

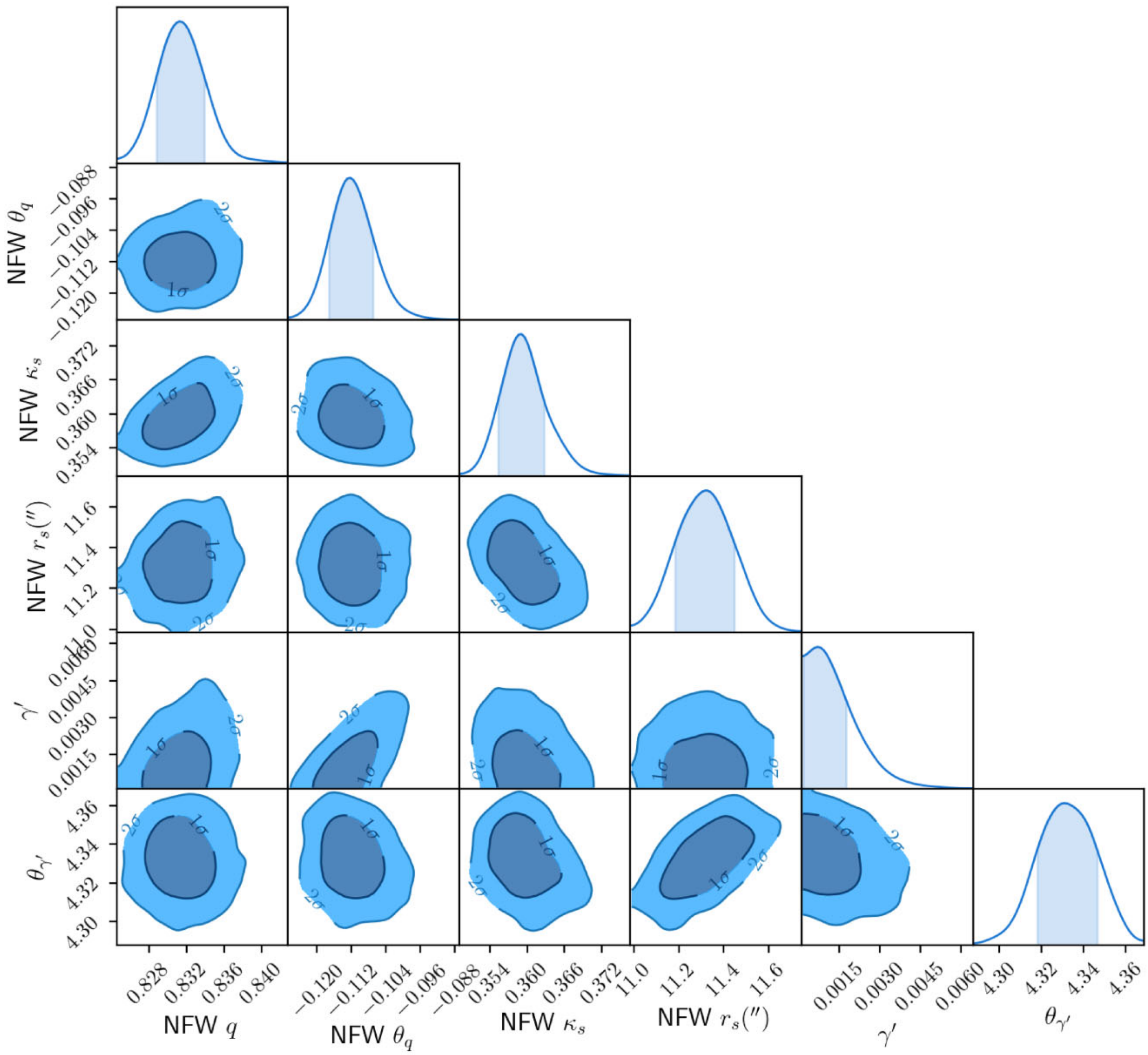


**Figure 6.** Marginalized parameter distributions from the J0924+0219 composite lens model results. NFW $q$ is axial ratio of NFW profile, NFW $\theta_q$ is the position angle of NFW, NFW $r_s$ is the scale radius of NFW profile, $\gamma'$ is the strength of the external shear, and $\theta_{\gamma'}$ is the orientation of the shear strength. The contours represent the 68.3 per cent and 95.4 per cent quantiles. Position angle is counterclockwise from +x in radians.

where $R$ is the projected radius, $I(R)$ is the light distribution, $\mathcal{P}$ is the PSF convolution kernel (Mamon & Łokas 2005), and $\mathcal{A}$ is the aperture. The streaming motions (e.g. rotation) are assumed to be zero. The luminosity-weighted line-of-sight velocity dispersion is given by

$$I(R)\sigma_s^2 = 2\int_R^\infty \left(1 - \beta_{\rm ani}\frac{R^2}{r^2}\right)\frac{\rho_* \sigma_r^2 r \,{\rm d}r}{\sqrt{r^2 - R^2}}. \quad (5)$$

The predicted velocity dispersion can be simplified and well approximated (Birrer et al. 2016, 2020; Chen et al. 2021b) as

$$\left(\sigma_v^{\rm p}\right)^2 = (1 - \kappa_{\rm ext})\lambda_{\rm int}\left(\frac{D_{\rm s}}{D_{\rm ds}}\right)c^2 J(\eta_{\rm lens}, \eta_{\rm light}, \beta_{\rm ani}), \quad (6)$$

where $J$ contains the angular-dependent information including the parameters describing the 3D deprojected mass distribution, $\eta_{\rm lens}$, the surface-brightness distribution in the lensing galaxy, $\eta_{\rm light}$, and the stellar orbital anisotropy distribution, $\beta_{\rm ani}$. $\kappa_{\rm ext}$ and $\lambda_{\rm int}$ represent the external MST and internal MST, respectively.

We assume the anisotropy component has the form of an anisotropy radius, $r_{\rm ani}$, in the Osipkov–Merritt (OM) formulation

**Table 5.** Lensing parameters for microlensing study. The values of $\kappa$, $\gamma$, and $\kappa_*/\kappa$ of J0924+0219 are from the composite model.

| Name | Img | $\kappa$ | $\gamma$ | $\kappa_*/\kappa$ |
|---|---|---|---|---|
| J0924+0219 | A | 0.312 | 0.600 | 0.234 |
| | B | 0.273 | 0.458 | 0.182 |
| | C | 0.378 | 0.828 | 0.194 |
| | D | 0.347 | 0.765 | 0.191 |

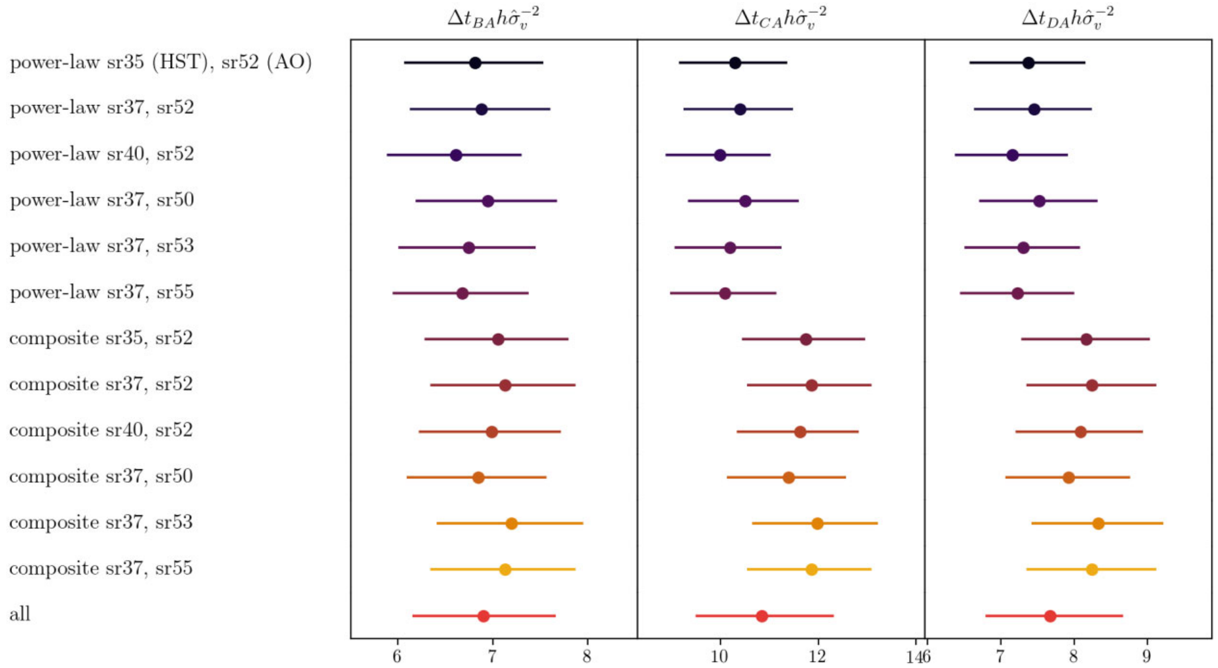


**Figure 7.** The predicted time delays from the power-law and composite models with different number of reconstructed source pixels for the *HST* imaging and AO imaging. 'sr35 (*HST*)' represents that we use source grid with 35 × 35 to reconstructed the background source of the *HST* imaging. All three bands of the *HST* imaging share the same number of reconstructed sources.

(Osipkov 1979; Merritt 1985),

$$\beta_{\rm ani} = \frac{r^2}{r_{\rm ani}^2 + r^2}, \tag{7}$$

where $r_{\rm ani} = 0$ is pure radial orbits and $r_{\rm ani} \rightarrow \infty$ is isotropic with equal radial and tangential velocity dispersions. In our models, we use a scaled version of the anisotropy parameter, $a_{\rm ani} \equiv r_{\rm ani}/r_{\rm eff}$, where $r_{\rm eff} = D_{\rm d}\theta_{\rm eff}$, and $\theta_{\rm eff}$ is the effective radius in angular units. Note that since the line-of-sight velocity dispersion has a degeneracy with the anisotropy parameters (Dejonghe 1987), we follow Chen et al. (2019) and marginalize the sample of $a_{\rm ani}$ over a uniform distribution [0.5, 5].

### 3.4 Time-delay prediction model

The predicted time delay can be expressed as

$$\Delta t = (1 - \kappa_{\rm ext})\lambda_{\rm int}\frac{D_{\Delta t}}{c}\Delta\phi(\theta, \beta), \tag{8}$$

where $c$ is the speed of light and $\theta$, $\beta$, and $\phi(\theta)$ are the image coordinates, the source coordinates, and the Fermat potential (Blandford & Narayan 1986) without the presence of internal or external MST, respectively. In the case of a single-aperture velocity dispersion, we can replace the MST terms ($\lambda_{\rm int}$ and $\kappa_{\rm ext}$) with equation (6) and the predicted time delays will directly relate to the velocity dispersion via

$$\Delta t = (1 + z_{\rm d})\frac{D_{\rm d}}{c}\frac{\Delta\phi(\theta, \beta)}{J(\eta_{\rm lens}, \eta_{\rm light}, a_{\rm ani})}\frac{\sigma_v^2}{c^2}. \tag{9}$$

The MST related terms (i.e. $\kappa_{\rm ext}$ and $\lambda_{\rm int}$) cancelled out in equation (9). Thus, the uncertainty of the predicted time delays does not depend on the uncertainty of the mass along the line of sight or transformed mass profile via MST, and only rely on the precision of the velocity dispersion measurement, the redshift of the lens, and the angular diameter distance to the lens (see also similar discussion in Koopmans 2006). In other words, once the time delay and velocity dispersion are measured, the value of $D_{\rm d}$ can be determined (Chen et al. 2021b). When further including environmental information (which provides an estimate of $\kappa_{\rm ext}$) and $D_{\rm s}/D_{\rm ds}$ information that comes from either external data sets or the assumption of a cosmological model, one can further determine $\lambda_{\rm int}$ (Birrer et al. 2020; Chen et al. 2021b) and use it to further constrain $H_0$ with $D_{\Delta t}$ from the population point of view (Birrer et al. 2020). Note that Birrer et al. (2020) use both $D_{\rm d}$ and $D_{\Delta t}$ information to constrain $H_0$.

## 4 PREDICTED TIME DELAYS IN ΛCDM COSMOLOGY

Because of the lack of velocity dispersion measurement for this lens, we express the observed velocity dispersion as $\sigma_v^{\rm ob} = \hat{\sigma}_v \times 280\,{\rm km\,s^{-1}}$, which is created by assuming a flat ΛCDM with fixed $\Omega_{\rm m} = 0.3$, $H_0 = 70\,{\rm km\,s^{-1}\,Mpc^{-1}}$, and $\lambda_{\rm int} = 1$ (i.e. no internal MST) in the power-law model (Chen et al. 2021b). We fold in an expected 5 per cent uncertainty of the velocity dispersion measurement and present time-delay predictions under the assumption of the ΛCDM model with fixed $\Omega_{\rm m} = 0.3$. For the velocity dispersion calculation, we assume the seeing is 1.0 arcsec and the aperture size is 1 × 1 arcsec$^2$. We show the predicted time delays in Fig. 7 with various source resolutions. When we marginalized over different source resolutions of the power-law model, the power-law model predicts $\Delta t_{\rm BA} = 6.75^{+0.78}_{-0.68}\,h^{-1}\hat{\sigma}_v^2$ d, $\Delta t_{\rm CA} = 10.2^{+1.2}_{-1.0}\,h^{-1}\hat{\sigma}_v^2$ d, and $\Delta t_{\rm DA} = 7.31^{+0.86}_{-0.74}\,h^{-1}\hat{\sigma}_v^2$ d. When we marginalized over different source resolutions of the composite model, the composite model predicts $\Delta t_{\rm BA} = 6.99^{+0.81}_{-0.71}\,h^{-1}\hat{\sigma}_v^2$ d, $\Delta t_{\rm CA} = 11.6^{+1.4}_{-1.2}\,h^{-1}\hat{\sigma}_v^2$ d, and $\Delta t_{\rm DA} = 8.10^{+0.96}_{-0.82}\,h^{-1}\hat{\sigma}_v^2$ d. When we marginalized power-law and composite models, we obtain $\Delta t_{\rm BA} = 6.89^{+0.78}_{-0.74}\,h^{-1}\hat{\sigma}_v^2$ d, $\Delta t_{\rm CA} = 10.7^{+1.6}_{-1.2}\,h^{-1}\hat{\sigma}_v^2$ d, and $\Delta t_{\rm DA} = 7.70^{+0.97}_{-0.91}\,h^{-1}\hat{\sigma}_v^2$ d. Given the expected short time delays in this system, it will be challenging to measure the time delays within 10 per cent uncertainty.

## 5 CONCLUSIONS

In this work, we use high-resolution Keck AO imaging data, collected by the SHARP team, and deep *HST* Wide Field Camera 3 (WFC3) images through the F160W filter, *HST* ACS/WFC images through F555W and F814W filters to simultaneously constrain the mass distribution of J0924+0219 lens system. When assuming a ΛCDM model with fixed $\Omega_{\rm m} = 0.3$, we find that the power-law model predicts $\Delta t_{\rm BA} = 6.75^{+0.78}_{-0.68}\,h^{-1}\hat{\sigma}_v^2$ d, $\Delta t_{\rm CA} = 10.2^{+1.2}_{-1.0}\,h^{-1}\hat{\sigma}_v^2$ d, and $\Delta t_{\rm DA} = 7.31^{+0.86}_{-0.74}\,h^{-1}\hat{\sigma}_v^2$ d; the composite model [i.e. a NFW dark matter halo (Navarro et al. 1996) plus a constant M/L ratio stellar distribution] predicts $\Delta t_{\rm BA} = 6.99^{+0.81}_{-0.71}\,h^{-1}\hat{\sigma}_v^2$ d, $\Delta t_{\rm CA} = 11.6^{+1.4}_{-1.2}\,h^{-1}\hat{\sigma}_v^2$ d, and $\Delta t_{\rm DA} = 8.10^{+0.96}_{-0.82}\,h^{-1}\hat{\sigma}_v^2$ d. When we marginalize over the power-law and composite models, we obtain $\Delta t_{\rm BA} = 6.89^{+0.78}_{-0.74}\,h^{-1}\hat{\sigma}_v^2$ d, $\Delta t_{\rm CA} = 10.7^{+1.6}_{-1.2}\,h^{-1}\hat{\sigma}_v^2$ d, and $\Delta t_{\rm DA} = 7.70^{+0.97}_{-0.91}\,h^{-1}\hat{\sigma}_v^2$ d. Future measurements of time delays with 10 per cent uncertainty and a velocity dispersion with 5 per cent uncertainty would yield a $H_0$ constraint of ∼15 per cent precision.

It is important to note that our analysis is *truly* blind since the time delays and velocity dispersion are not yet measured. Once the velocity dispersion and time delays are measured, the derived posteriors can be used to constrain the $H_0$. As part of the TDCOSMO effort, we are obtaining measurements of this lens in order to have a high-quality $H_0$ measurement under the assumptions of standard NFW profile and fixed M/L ratio. These assumptions are in general supported by Shajib et al. (2021) and are currently the standard in the TDCOSMO Collaboration. Future works that include varying M/L ratio, allowing for contracted/expanded NFW profiles, and adapting axisymmetric Jeans equations are worth examining once spatially resolved kinematics data are obtained.

## ACKNOWLEDGEMENTS

GC-FC thanks Simon Birrer, Dominique Sluse, Aymeric Galan, and Elizabeth Buckley-Geer for many insightful comments. GC-FC, CDF, and TT acknowledge support by the National Science Foundation through grants NSF-AST-1907396 and NSF-AST-1906976 ‘Collaborative Research: Toward a 1 per cent Measurement of the Hubble Constant with Gravitational Time Delays’, NSF-1836016 ‘Astrophysics Enabled by Keck All Sky Precision Adaptive Optics’, and NSF-AST-1715611 ‘Collaborative Research: Investigating the Nature of Dark Matter with Gravitational Lensing’. We also acknowledge support by the Gordon and Betty Moore Foundation Grant 8548 ‘Cosmology via Strongly Lensed Quasars with KAPA’. SHS thanks the Max Planck Society for support through the Max Planck Research Group, and is supported in part by the Deutsche Forschungsgemeinschaft (DFG, German Research Foundation) under Germany’s Excellence Strategy – EXC-2094 – 390783311.

## DATA AVAILABILITY

The data underlying this paper will be shared on reasonable request to the corresponding author.

## REFERENCES

Anderson L. et al., 2014, MNRAS, 441, 24
Auger M. W., Treu T., Bolton A. S., Gavazzi R., Koopmans L. V. E., Marshall P. J., Moustakas L. A., Burles S., 2010, ApJ, 724, 511
Badole S., Jackson N., Hartley P., Sluse D., Stacey H., Vives-Arias H., 2020, MNRAS, 496, 138
Barkana R., 1998, ApJ, 502, 531
Barnabè M., Czoske O., Koopmans L. V. E., Treu T., Bolton A. S., 2011, MNRAS, 415, 2215
Binney J., Tremaine S., 1987, Galactic Dynamics. Princeton Univ. Press, Princeton, NJ
Birrer S., Treu T., 2021, A&A, 649, A61
Birrer S., Amara A., Refregier A., 2016, J. Cosmol. Astropart. Phys., 08, 020
Birrer S. et al., 2019, MNRAS, 484, 4726
Birrer S. et al., 2020, A&A, 643, A165
Blandford R., Narayan R., 1986, ApJ, 310, 568
Blum K., Castorina E., Simonović M., 2020, ApJ, 892, L27
Bolton A. S., Burles S., Schlegel D. J., Eisenstein D. J., Brinkmann J., 2004, AJ, 127, 1860
Bolton A. S., Burles S., Koopmans L. V. E., Treu T., Moustakas L. A., 2006, ApJ, 638, 703
Bonvin V., Tewes M., Courbin F., Kuntzer T., Sluse D., Meylan G., 2016, A&A, 585, A88
Bradač M., Schneider P., Steinmetz M., Lombardi M., King L. J., Porcas R., 2002, A&A, 388, 373
Cappellari M. et al., 2015, ApJ, 804, L21
Chen G. C.-F. et al., 2016, MNRAS, 462, 3457
Chen G. C.-F. et al., 2018, MNRAS, 481, 1115
Chen G. C.-F. et al., 2019, MNRAS, 490, 1743
Chen G. C.-F., Treu T., Fassnacht C. D., Ragland S., Schmidt T., Suyu S. H., 2021a, MNRAS, 508, 755
Chen G. C.-F., Fassnacht C. D., Suyu S. H., Yıldırım A., Komatsu E., Luis Bernal J., 2021b, A&A, 652, A7
Collett T. E. et al., 2013, MNRAS, 432, 679
Courbin F. et al., 2018, A&A, 609, A71
Dalal N., Kochanek C. S., 2002, ApJ, 572, 25
Dejonghe H., 1987, MNRAS, 224, 13
Ding X. et al., 2021, MNRAS, 503, 1096
Dutton A. A., Treu T., 2014, MNRAS, 438, 3594
Dutton A. A. et al., 2011, MNRAS, 417, 1621
Eigenbrod A., Courbin F., Dye S., Meylan G., Sluse D., Vuissoz C., Magain P., 2006, A&A, 451, 747
Falco E. E., Gorenstein M. V., Shapiro I. I., 1985, ApJ, 289, L1
Fassnacht C. D., Xanthopoulos E., Koopmans L. V. E., Rusin D., 2002, ApJ, 581, 823
Faure C., Sluse D., Cantale N., Tewes M., Courbin F., Durrer P., Meylan G., 2011, A&A, 536, A29
Freedman W. L. et al., 2019, ApJ, 882, 34
Freedman W. L. et al., 2020, ApJ, 891, 57
Gavazzi R., Treu T., Rhodes J. D., Koopmans L. V. E., Bolton A. S., Burles S., Massey R. J., Moustakas L. A., 2007, ApJ, 667, 176
Gilman D., Birrer S., Treu T., 2020, A&A, 642, A194
Glikman E., Rusu C. E., Djorgovski S. G., Graham M. J., Stern D., Urrutia T., Lacy M., O’Meara J. M., 2018, AJ, preprint (arXiv:1807.05434)
Gorenstein M. V., Falco E. E., Shapiro I. I., 1988, ApJ, 327, 693
Greene Z. S. et al., 2013, ApJ, 768, 39
Hernquist L., 1990, ApJ, 356, 359
Hinshaw G. et al., 2013, ApJS, 208, 19
Inada N. et al., 2003, AJ, 126, 666
Jee I., Komatsu E., Suyu S. H., 2015, J. Cosmol. Astropart. Phys., 11, 033
Jee I., Komatsu E., Suyu S. H., Huterer D., 2016, J. Cosmol. Astropart. Phys., 04, 031
Jee I., Suyu S. H., Komatsu E., Fassnacht C. D., Hilbert S., Koopmans L. V. E., 2019, Science, 365, 1134
Kazin E. A. et al., 2014, MNRAS, 441, 3524
Kochanek C. S., 2020, MNRAS, 493, 1725
Kochanek C. S., 2021, MNRAS, 501, 5021
Komatsu E. et al., 2011, ApJS, 192, 18
Koopmans L. V. E., 2006, in Mamon G. A., Combes F., Deffayet C., Fort B., eds, EAS Publ. Ser. Vol. 20, Mass Profiles and Shapes of Cosmological Structures. EDP Sciences, Paris, p. 161
Koopmans L. V. E. et al., 2003, ApJ, 595, 712

Koopmans L. V. E., Treu T., Bolton A. S., Burles S., Moustakas L. A., 2006, ApJ, 649, 599
Koopmans L. V. E. et al., 2009, ApJ, 703, L51
Krist J. E., Hook R. N., 1997, in Casertano S., Jedrzejewski R., Keyes C. D., Stevens M., eds, The 1997 HST Calibration Workshop with a New Generation of Instruments. Space Telescope Science Institute, Baltimore, MD, p. 192
Mamon G. A., Łokas E. L., 2005, MNRAS, 363, 705
Merritt D., 1985, AJ, 90, 1027
Metcalf R. B., Madau P., 2001, ApJ, 563, 9
Millon M. et al., 2020, A&A, 639, A101
Navarro J. F., Frenk C. S., White S. D. M., 1996, ApJ, 462, 563
Osipkov L. P., 1979, Pisma Astron. Zh., 5, 77
Planck Collaboration VI, 2020, A&A, 641, A6
Pooley D., Rappaport S., Blackburne J. A., Schechter P. L., Wambsganss J., 2012, ApJ, 744, 111
Refsdal S., 1964, MNRAS, 128, 307
Riess A. G., Casertano S., Yuan W., Macri L. M., Scolnic D., 2019, ApJ, 876, 85
Ross A. J., Samushia L., Howlett C., Percival W. J., Burden A., Manera M., 2015, MNRAS, 449, 835
Rusu C. E., Berghea C. T., Fassnacht C. D., More A., Seman E., Nelson G. J., Chen G. C. F., 2019, MNRAS, 486, 4987
Schechter P. L., Pooley D., Blackburne J. A., Wambsganss J., 2014, ApJ, 793, 96
Schneider P., Sluse D., 2013, A&A, 559, A37
Shajib A. J. et al., 2020, MNRAS, 494, 6072
Shajib A. J., Treu T., Birrer S., Sonnenfeld A., 2021, MNRAS, 503, 2380
Sonnenfeld A., Treu T., Gavazzi R., Marshall P. J., Auger M. W., Suyu S. H., Koopmans L. V. E., Bolton A. S., 2012, ApJ, 752, 163
Sonnenfeld A., Treu T., Gavazzi R., Suyu S. H., Marshall P. J., Auger M. W., Nipoti C., 2013, ApJ, 777, 98
Suyu S. H., Halkola A., 2010, A&A, 524, A94
Suyu S. H., Marshall P. J., Hobson M. P., Blandford R. D., 2006, MNRAS, 371, 983
Suyu S. H., Marshall P. J., Blandford R. D., Fassnacht C. D., Koopmans L. V. E., McKean J. P., Treu T., 2009, ApJ, 691, 277
Suyu S. H. et al., 2012, ApJ, 750, 10
Suyu S. H. et al., 2013, ApJ, 766, 70
Suyu S. H. et al., 2014, ApJ, 788, L35
Suyu S. H. et al., 2017, MNRAS, 468, 2590
Taubenberger S. et al., 2019, A&A, 628, L7
Treu T., Koopmans L. V. E., 2002, MNRAS, 337, L6
Treu T., Marshall P. J., 2016, A&AR, 24, 11
Treu T. et al., 2018, MNRAS, 481, 1041
Wong K. C. et al., 2017, MNRAS, 465, 4895
Wong K. C. et al., 2020, MNRAS, 498, 1420
Xu D., Sluse D., Schneider P., Springel V., Vogelsberger M., Nelson D., Hernquist L., 2016, MNRAS, 456, 739

This paper has been typeset from a TEX/LATEX file prepared by the author.